Atmospheric
Measurement
Techniques
Discussions

EGU

An overview and issues of the sky radiometer technology and SKYNET

Teruyuki Nakajima[1], Monica Campanelli[2], Huizheng Che[3], Victor Estellés[2,4], Hitoshi Irie[5], Sang-Woo Kim[6], Jhoon Kim[7], Dong Liu[8], Tomoaki Nishizawa[9], Govindan Pandithurai[10], Vijay Kumar Soni[11], Boossarasiri Thana[12], Nas-Urt Tugjsurn[13], Kazuma Aoki[14], Makiko Hashimoto[1], Akiko Higurashi[9], Stelios Kazadzis[15], Pradeep Khatri[16], Natalia Kouremeti[15], Rei Kudo[17], Franco Marenco[18], Masahiro Momoi[5,19], Shantikumar S. Ningombam[20], Claire L. Ryder[21], Akihiro Uchiyama[9]

[1]Japan Aerospace Exploration Agency; 2-1-1 Sengen, Tsukuba, Ibaraki 305-8505, Japan
[2]Consiglio Nazionale delle Ricerche, Istituto Scienze dell'Atmosfera e del Clima; via Fosso del Cavaliere, 100, 00133 - Roma, Italy
[3]Centre for Atmosphere Watch And Services, CMA Chinese Academy of Meteorological Sciences; 46 Zhong-Guan-Cun S. Ave., Beijing 100081, China
[4]Dept. Física de la Terra i Termodinàmica, Universitat de València; Burjassot, Valencia, Spain
[5]Center for Environmental Remote Sensing, Chiba University; Chiba 263-8522, Japan
[6]School of Earth and Environmental Sciences, Seoul National University; 08826, Seoul, Republic of Korea
[7]Dept. of Atmospheric Sciences, Yonsei University, Seoul 03722, Republic of Korea
[8]Center for Atmospheric Optics, Anhui Institute of Optics and Fine Mechanics, Hefei Institutes of Physical Science, Chinese Academy of Sciences; Hefei, Anhui 230031, China
[9]National Institute for Environmental Studies; 16-2 Onogawa, Tsukuba, Ibaraki 305-8506, Japan
[10]Centre for Climate Change Research, Indian Institute of Tropical Meteorology; Pune 411 008, India
[11]Environment Monitoring & Research Centre, India Meteorological Department; Mausam Bhawan, Lodi Road, New Delhi-110003, India
[12]Thailand Global Warming Academy, Napamitr Foundation; 234/88 Asoke-Din Daeng Road, Bang Kapi Sub-district, Huai Khwang District, Bangkok 10310, Thailand
[13]Physics department, Mongolian University of Science and Technology; 216046, Ulaanbaatar, Mongolia
[14]Graduate School of Science and Engineering (Science), University of Toyama; 3190 Gofuku, Toyama 930-8555, Japan
[15]Physikalisch-Meteorologisches Observatorium Davos, World Radiation Center, Dorfstrasse 33, CH-7260 Davos Dorf, Switzerland
[16]Center for Atmospheric and Oceanic Studies, Graduate School of Science, Tohoku University, Sendai, Japan
[17]Meteorological Research Institute, Meteorological Agency; Nagamine, Tsukuba 305-0052, Ibaraki, Japan
[18]Satellite Applications, Met Office, United Kingdom
[19]Graduate School of Science, Tokyo University of Science, Tokyo 162-8601, Japan
[20]Indian Institute of Astrophysics, 2nd Block Koramangala, Bangalore 560034, India
[21]Department of Meteorology, University of Reading, Reading, RG6 6BB, United Kingdom

Correspondence to: T. Nakajima (terry-nkj@nifty.com)

Abstract. This paper overviews the progress in the sky radiometer technology and development of the network called SKYNET. It is found that the technology has produced useful on-site calibration methods, retrieval algorithms, and data analyses from the sky radiometer observation of aerosol, cloud, water vapor and ozone. Increasing collaborations of users in the SKYNET community are becoming a useful platform for research and operation. The paper also presents issues of the technology for future development.

Atmospheric
Measurement
Techniques
Discussions

1 Introduction

A sun–sky radiometer is a narrow band filter photometer able to perform measurements of direct solar and diffuse sky radiation at selected wavelengths and at several scattering angles. Observed data have large information contents for aerosol,
5   cloud, and gaseous constituents, but are difficult to retrieve because of the need for full radiative transfer computation to quantify single and multiple scattered radiation.

The origin of the idea of the technology dates back to 1920s. Long-term direct solar and diffuse sky measurements were carried out during 1923-1957 by the Smithsonian Astronomical Observatory by monitoring the solar constant with a pyrheliometer at Montezuma (Chile) and Table Mountain (California) (Ångström, 1961, 1974; Hoyt, 1979a, b). Diffuse sky
10   irradiance in the circumsolar or solar aureole region was measured by the pyranometer to correct for the atmospheric effects in the measured solar constant. In the 1970s, spectral measurements of the direct solar radiation became popular for air pollution monitoring by introduction of a low cost compact narrow band radiometer called a sunphotometer with a silicon photodiode and cutoff or interference optical filters (Volz, 1959, 1974). In parallel, pioneering measurements of the spectral diffuse sky radiance, especially in the circumsolar region, started (Eiden, 1968; Green et al., 1971; Twitty, 1975).
15   Combined analyses of sun and sky radiation data were not attained until the 1980s (e.g., O'Neill and Miller, 1984a, b; Tanaka et al., 1986; Tanré et al., 1988) after the full radiative transfer computation became possible, allowing quantification of the multiple scattering component of sky radiance and retrieval of the column-averaged size distribution and the complex refractive index of polydispersed aerosol (Deirmendjian, D., 1957, 1959; Dave, 1971; Twitty, 1975; Weinman et al., 1975; Box and Deepak, 1978, 1979; Nakajima et al., 1983; O'Neill and Miller, 1984b; Tanré et al., 1988; Tonna et al., 1995;
20   Dubovik and King, 2000; Dubovik et al., 2000, 2002). Networks of the radiometer have been developed to utilize sun and sky measurement data for various applications such as satellite remote sensing validation, air pollution monitoring and study of climate effects of atmospheric constituents. The largest network is the NASA AERONET (Holben et al., 1998) developed in the early 1990s and currently with more than 500 radiometers named the sun-sky photometer. Later in around the 2000s, SKYNET was formed with the sky radiometer (Nakajima et al., 2007). Compared to the AERONET technology, SKYNET
25   has several differences in measurement and analysis methods, which are useful to overview and assess for the world community to understand the system, which is the purpose of this paper.

2. Sun and sky measurements by the sky radiometer

The SKYNET is a research group of users of the sky radiometer initiated around the time of the East Asian Regional Experiment (EAREX) 2005 (Nakajima et al., 2007), one of the regional experiments under the UNEP Atmospheric Brown
30   Cloud (ABC) project (Ramanathan et al., 2007). A number of sky radiometers were deployed in the East Asian region for

measuring the aerosol optical properties in order to estimate the aerosol impact on the earth's radiation budget (Takamura et al., 2004). Since then, the network has kept growing in the world and the number of sky radiometers now exceeds 100 units. Table 1 and Fig. 1 show the sky radiometer sites as recognized by the International Skynet Committee (ISC). Users established regional sub-network groups in China, Europe, India, Japan, Korea, Mongolia, and South East Asia for data

5   analysis and formed the ISC to discuss international collaboration issues (Fig.2). Historically two major groups were grown for regional data collection and analysis: the Center for Environmental Remote Sensing (CEReS) of Chiba University (Takamura et al., 2004, 2009, 2013) and the European Skynet Radiometers network (ESR) (Campanelli et al, 2004, 2007, 2012). In 2017, the SKYNET has become a contributing network of the WMO Global Atmospheric Watch (GAW). In this expanding situation of SKYNET with more burden and responsibility, the ISC decided to establish the International

10   SKYNET Data Center (ISDC) at the National Institutes for Environmental Studies (NIES) in Japan to start a shared data collection and analysis based on the MOU between users and the ISDC. Among the sites in Table 1, the ISDC is starting receiving data from 25 sites in the world. The ISDC is going to provide standard products from the SKYNET network, whereas the regional sub-networks will develop new research products and test new methodologies.

The main instrument of the SKYNET is the sky radiometer manufactured by PREDE Co. Ltd. Several versions of the

15   radiometer have been made by user's requests. POM01 is the standard version with seven wavelengths of $\lambda = 315, 400, 500, 675, 870, 940$ and 1020 nm and POM02 is an extended version with UV wavelengths of 340nm and 380nm, and shortwave infrared wavelengths of 1600nm and 2200nm. Channels of 315nm and 940nm are installed for ozone and water vapor amount retrievals. There is a modified version of POM02 for lunar photometry (Uchiyama et al., 2019). Shipborne versions have been also built (Kobayashi and Shiobara, 2015).

20   Sky radiometer readings of direct solar and diffuse sky measurements, V_d and V_s, are related to the direct solar irradiance F_d and sky radiance $\overline{L}_s$ at the mean earth's orbit as,

$$F_d = C_R R_{es}^2 V_d, \quad \overline{L}_s = \frac{F_s}{\Delta\Omega} = C_R \frac{R_{es}^2 V_s}{\Delta\Omega} \quad , \tag{1}$$

where C_R is the radiometric sensitivity or calibration coefficient of the radiometer to translate the radiometer reading to irradiance unit, say Wm^{-2} nm^{-1}; $\Delta\Omega$ is the Solid Viewing Angle (SVA) of the radiometer; R_{es} is the sun-earth distance in the

25   astronomical unit. SKYNET remote sensing uses the beam transmittance T_d of the atmosphere and relative sky radiance R (Nakajima et al., 1986) defined as,

$$T_d \equiv \frac{F_d}{F_0} = \exp(-m_0\tau), \tag{2a}$$

$$\tau = \tau_a + \tau_m, \quad \omega\tau = \omega_a\tau_a + \omega_m\tau_m \quad , \tag{2b}$$

$$R(\theta,\phi;\theta_0,\phi_0) \equiv \frac{\overline{L}_s(\theta,\phi;\theta_0,\phi_0)/m}{F_d} = \frac{1}{m\Delta\Omega}\frac{V_s}{V_d}, \tag{2c}$$

where τ is the Optical Thickness (OT) of the atmosphere consisting of molecular optical thickness τ_m and Single Scattering Albedo (SSA) ω_m, and Aerosol Optical Thickness (AOT) τ_a and SSA ω_a in the clear sky condition; F_0 is the Extraterrestrial Solar Irradiance (ESI); (θ_0, ϕ_0) and (θ, ϕ) are zenith and azimuthal angles of the sun and the line of sight of the sky radiometer, respectively; m_0 and m are optical airmasses for solar insolation and line of sight of the radiometer, which are

5   approximated as $1/\cos(\theta_0)$ and $1/\cos(\theta)$ for plane-parallel geometry of the atmosphere. All the radiative quantities are measured by band-pass filters of widths about 10nm. SKYNET adopts on-site calibration routines to determine the two radiometric constants, F_0 and $\Delta\Omega$, by the Improved Langley plot method (hereafter, IL or IL plot method) and the disk scan method (Nakajima et al, 1996; Boi et al., 1999) as discussed in Sections 3 and 4. Under the condition that C_R and F_0 do not change between time of measurement and time of F_0 determination, T_d and R do not depend on the calibration coefficient C_R,

10   so that we can select the radiometer reading for F_0, i.e. $C_R=1$, without the absolute radiometric calibration. In order to meet this condition, therefore, the on-site calibration is required to be performed as frequent as possible to monitor change of C_R due to machine condition change and F_0 change due to solar luminosity change.

Once the radiometric constants are determined, the direct solar irradiance F and relative sky radiance R are used for the Level-2 (L2) analysis, i.e., retrievals of the geophysical parameters of aerosol, cloud, water vapor and ozone as discussed

15   later in Section 5. The flow of sky radiometer measurements and data analysis are schematically depicted in Fig. 3. As overviewed in the following sections, F_0 and SVA are obtained on site through the various Langley plot methods and solar disk scan method using data from direct solar and forward scan measurements. Cloud screening is also performed with frequent direct solar measurements similar to AERONET method (Estellés et al., 2012; Song et al., 2014). Although not on a regular routine, SKYNET participates inter-radiometer comparisons and high mountain measurements. A lamp scan method

20   has been tried from 2016 at the CEReS site as described in Section 4. To obtain data for L2 data analysis for retrieval of geophysical parameters for atmospheric constituents, an analysis software called Skyrad.pack has been developed (Nakajima et al., 1996; Hashimoto et al., 2012) and publicly opened on the OpenCLASTR shareware site (http://157.82.240.167/~clastr/data_policy.html) for the research community. Various L2 products are retrieved by the Skyrad.pack   such as spectra of AOT and SSA, its slope called Ångström exponent (AE), size distribution function (SDF),

25   asphericity, Cloud Optical Thickness (COT), Cloud Effective particle Radius (CER), and water/ice phase from data in the non-gas absorbing channels, column water vapor (W) and column ozone amount (U) from the gas absorbing channels, as explained in the following sections.

3. Radiometric calibration of the direct solar irradiance measurements

In the case of non-gas absorption channels, the Standard Langley plot method (SL or SL plot method) can be used to obtain

30   F_0 by plotting the logarithm of the Lambert-Beer's law Eq. (2a) versus m_0,

$$\ln F_d = \ln F_0 - m_0 \tau \,, \tag{3}$$

to extrapolate the linear regression line to $m_0 = 0$. It is known, however, that an airmass dependence or a quadratic time dependence of AOT introduces a serious error in the SL as claimed by Shaw (1976). Correction methods to this problem were proposed by O'Neill and Miller (1984a, b) and Tanaka et al. (1986) with use of a time dependence of the circumsolar radiance of which the major part is approximated by the single scattered radiance proportional to the OT along the solar almucantar circle ($\theta = \theta_0$), given as,

$$R(\theta,\phi;\theta_0,\phi_0) = \omega\tau P(\Theta) + R_{mult}(\theta,\phi;\theta_0,\phi_0), \tag{4}$$

where P is the normalized scattering phase function at the scattering angle of Θ and R_{mult} is the multiple scattered radiation. Tanaka et al. (1986) used a forward scattering around $\Theta = 20°$ at which the phase function is relatively independent of the SDF of the atmospheric particulate matter. Extending this principle, SKYNET adopts the IL method to extrapolate Eq. (3) regarding the total scattering optical path,

$$x = m_0\omega\tau, \tag{5a}$$

or its aerosol part,

$$x_a = m_0\omega_a\tau_a, \tag{5b}$$

which can be retrieved from the forward scattering part of the normalized sky radiance R, Eq.(4). The formulae in Eqs. (4) and (5) indicate that x_a is relatively accurately retrieved from the inversion of the forward scattering part of the sky radiance. The accuracy of F_0 estimation by the IL method depends on the turbidity condition of the site. The theory of a linear regression model is formulated with a normal random observation error u in the case of adopting an expression of Eq. (5a) as,

$$y_i = a + bx_i + u_i, \quad i = 1,...n, \tag{6a}$$

$$a = \ln F_0, \quad x = m_0\omega\tau, \quad y = \ln(F), \tag{6b}$$

where n is the number of observations. Equation 6 gives estimates of regression coefficients and their dispersion as,

$$b = \frac{<(x-\bar{x})(y-\bar{y})>}{\sigma_x^2}, \quad a = \bar{y} - b\bar{x}, \tag{7a}$$

$$\sigma_b^2 = \frac{\varepsilon_u^2}{n\sigma_x^2}, \quad \sigma_a^2 = \frac{\varepsilon_u^2}{n}(1+\frac{\bar{x}^2}{\sigma_x^2}), \tag{7b}$$

where upper bar and $<>$ stand for averaging operation. The standard linear regression theory assumes x is an independent variable to be related to a dependent variable y which includes random residual of the fitting u. Based on this assumption, the dispersion of x is given as,

$$(\frac{\sigma_x}{\bar{x}})^2 \sim \frac{\sigma_{m0}^2}{\bar{m}_0^2} + \frac{\sigma_\tau^2}{\bar{\tau}^2} + \frac{\sigma_\omega^2}{\bar{\omega}^2}, \tag{8a}$$

Atmospheric
Measurement
Techniques

Open Access

Discussions

where σ_{m0}^2, σ_τ^2 and σ_ω^2 are dispersions of sampling airmasses $\{m_{0i}\}$, natural variations in $\{\tau_i\}$ and $\{\omega\}$ during the IL plot measurements, respectively. The dispersion of residual $\{u_i\}$ is approximated by the sum of mean square errors of τ and ω, i.e. ε_τ^2 and ε_ω^2, caused by the inversion process of Eq. (4) as,

$$\varepsilon_u^2 = b^2 \bar{m}_0^2 [(\bar{\omega}\varepsilon_\tau)^2 + (\bar{\tau}\varepsilon_\omega)^2] + \varepsilon_F^2, \tag{8b}$$

5

where ε_F^2 is the mean square error of $\{y_i\}$ caused by observation by the radiometer, which is usually small and neglected from the formula. The budget of dispersions Eq. (8a) leads to the following estimate for a typical airmass sampling from $m_1 = 1.3$ to $m_2 = 3.5$ and atmospheric conditions of large optical parameter change from $\tau_1 = 0.2$ to $\tau_2 = 0.4$, and from $\omega_1 = 0.85$ to $\omega_2 = 0.95$ during the IL plot as,

$$\left(\frac{\sigma_x}{\bar{x}}\right)^2 \approx \frac{1}{3}\left(\frac{m_2 - m_1}{m_2 + m_1}\right)^2 + \frac{1}{3}\left(\frac{\tau_2 - \tau_1}{\tau_2 + \tau_1}\right)^2 + \frac{1}{3}\left(\frac{\omega_2 - \omega_1}{\omega_2 + \omega_1}\right)^2 = 0.070 + 0.037 + 0.001, \tag{9}$$

10

if we assume a regular sampling of linear change models for m, τ, and ω. This budget indicates that the wide sampling of airmass is the main contributor to decrease σ_a^2. The IL method allows selection of the atmospheric condition in which τ and ω undergo natural variations that help to increase σ_x and thus decrease σ_a. But such selection of unstable atmospheric conditions may increase inversion errors, ε_τ and ε_ω, waisting the benefit of natural changes in ω and τ. Combining Eqs. (7) and (8), we have the following estimate for σ_a assuming b and ω are close to 1,

15

$$\sigma_{a,IL} = \frac{3.5}{\sqrt{n}} \frac{\bar{m}_0^2}{|m_2 - m_1|} \bar{\tau} \sqrt{\left(\frac{\varepsilon_\tau}{\bar{\tau}}\right)^2 + \left(\frac{\varepsilon_\omega}{\bar{\omega}}\right)^2} \sim \frac{1.3}{\sqrt{n}} \bar{\tau}. \tag{10}$$

The rightmost expression is an estimate for $m_1 = 1.3$, $m_2 = 3.5$ and 10% relative errors in inversion of τ and ω as a typical example of IL plot. This estimate indicates the accuracy of $\ln(F_0)$ from the IL method is proportional to the OT at the site. We can get 1 to 2% accuracy of F_0 if we can get $n=50$ to 100, say 10 clear days with 10 airmasses per IL plot under conditions of $\tau=0.1$. This error estimate is comparable to the RMSD of 1 to 2% regardless of wavelength in the F_0-time series obtained by the ESR data analysis with 30 to 60 days calibration period with the IL method (Campanelli et al., 2004, 2007).

20

This monitoring ability of F_0 by IL on site has merits such as low cost, frequent calibration to detect the changing constants and a short-term ESI change, and minimizing the radiometer environmental change avoiding shipping for calibration. The error in F_0 is propagated to cause an error in OT from Eq. (3) as,

25

$$\varepsilon_{direct,\tau} \sim \frac{\sigma_a}{m_0}. \tag{11}$$

A rough estimate of OT error by the IL calibration, caused by F_0 with n=50 to 100 for example, is expected to be of the order 0.005 to 0.01 from Eq. (10), though real errors depend on detailed setup and observation sequence at each site. It is important to compare this accuracy of IL with that of SL. In the SL case, we assume $x=m$ in Eq. (6a), so that the error estimate Eq. (7b) is reduced to the following expression as,

$$5 \quad \sigma_{a,SL}^2 = \frac{\tau'^2}{n}(1+\frac{\bar{m}^2}{\sigma_m^2}), \qquad (12a)$$

where we assume the error in a is caused by a part of OT change during the SL plot which tends to the inverse of the optical airmass as,

$$\tau = \bar{\tau} + \frac{\tau'}{m}. \qquad (12b)$$

A measure of OT change during airmass change from m_1 to m_2 can be defined as

$$10 \quad \delta_\tau \equiv \frac{\tau_1 - \tau_2}{2} = \frac{1}{2}(\frac{1}{m_2} - \frac{1}{m_1})\tau' = 0.24\tau'. \qquad (12c)$$

The rightmost estimate is given for m_1=1.3 and m_2=2.5 as an example. If we assume $\delta_\tau/\bar{\tau} = 0.1$ as same as inversion error in the estimate of IL accuracy, the following estimate is given as,

$$\sigma_{a,SL} = \frac{1.6}{\sqrt{n}}\bar{\tau}. \qquad (13)$$

This estimate of the SL error is similar to that of IL given in Eq. (10), suggesting the SL performance is similar to or slightly

15 larger than that of IL under conditions of 10% change in OT during the SL plot. Selection of the calibration methods, therefore, depends on the character of the turbidity conditions at the site. There are reports from city-area sites, such as Rome, Beijing and Chiba city, that the accuracy of SL method exceeds 1 to 2% worse than that of IL method, suggesting $\delta_\tau/\bar{\tau} > 0.1$ commonly happens at these sites, so that we recommend comparison of F_0 values from both SL and IL methods to diagnose the calibration quality of the IL method. At the same time, we recommend high mountain calibration and/or

20 transfer of calibration constants from a well-calibrated standard radiometer to keep the on-site IL calibration healthy.
The SKYNET community performed high mountain calibrations at Mauna Loa (USA, 3397mMSL) and from two similar pristine aged-background sites (AOT~0.05 at 500nm), Indian Astronomical Observatory (IAO), Hanle (Mt. Saraswati, 32°47'N, 78°58'E, 4500m MSL) and Merak (33°48'N, 78°37'E, 4310m MSL), located in the high-altitude Ladakh region in the north-western Himalaya. Figure 4 shows retrieved values of F_0 and SVA from the observation taken by a single

25 instrument (POM-01) from IAO-Hanle during January 2008- December 2010 and June 2015-December 2018 and Merak during January 2011-May 2015. The figure indicates the RMSD of $\ln(F_0)$ from SL and IL methods agree within about 0.005, which is consistent with an estimate Eqs. (10) and (13) assuming the mean AOT at the site of order of 0.03 at λ= 500nm and n= 100. The figure shows that the disk scan method, discussed in the next section, was obtained with monthly mean SVA within 1.5% for all the spectral channels. The disk scan was performed from observations taken under full clear sky

Atmospheric
Measurement
Techniques
Discussions

conditions with minimum 3-5 days data in every month (Ningombam et al., 2014). Therefore, there are 12 values of SVA in all the spectral channels in a year. The vertical bar indicates a representative RMSD of monthly means in each year.

The first QUAlity and TRaceabiliy of Atmospheric aerosol Measurements (QUATRAM, http://www.euroskyrad.net/quatram.html) Campaign compared the F_0-value from IL method with that of the standard

5   Precision Filter Radiometer (PFR) (Kazadzis et al., 2018b) of the World optical depth Research and Calibration Center (PMOD/WRC). A preliminary analysis showed the difference is 0.3% at Davos (1590m MSL) where the mean AOT is 0.15 and AOT in clean aerosol conditions is 0.05 at 500nm, indicating the importance of the careful constant calibration effort. Another important point to note is that comparison of Eqs. (3) and (6) lead to the following relation,

$$b = -\frac{1}{\omega} \ . \tag{14}$$

10 The forward scattering analysis of the IL method prescribes the refractive index, so that it is highly possible for x in Eq. (5a) to include a factor type systematic error like,

$$x = Cx_0 \ . \tag{15a}$$

In this case, Eq. (6) results in the following relation between fitted and true values of a and b, a_0 and b_0, as

$$b = \frac{1}{C}b_0, \quad a = \overline{y} - \frac{1}{C}b_0 C\overline{x}_0 = \overline{y} - b_0\overline{x}_0 \ . \tag{15b}$$

15 This result shows that the formula of a in Eq. (7a) is invariant to the factor type error indicating the robustness of the IL calibration. On the other hand, b-value changes depending on the value of C and takes the true value $-1/\omega$ according to Eq. (16). Boi et al. (1999) utilized this point and proposed an iterative IL method to improve the F_0-value and find the optimum complex refractive index by trying several refractive indices. They reported the Boi method can improve the precision of F_0 by 30%, e.g. 2% to 1.5%.

20 There is another caution regarding use of the formulae Eq. (7a). In the real observation, it is difficult to separate natural variations and inversion errors of τ and ω, so that the dispersion σ_x tends to include undesired inversion errors, that lead the IL method to underestimation of a and b as understood by Eq. (7b). We are testing a new solution to this problem, named the cross IL method (XIL), which exchanges the role of x and y in the regression analysis, i.e.,

$$x_i = \alpha + \beta y_i + v_i, \quad i = 1,...n \ , \tag{16a}$$

25 $$b = \frac{1}{\beta}, \quad a = -\frac{\alpha}{\beta} \ . \tag{16b}$$

Figure 5 presents retrieved values of a ($=\ln F_0$) from IL and XIL methods with ten ensemble runs of an idealized experiment with $F_0=1$, $\omega=1$, $\tau=0.1$; $n=20$ and $m=1.3$ to 3.5 as a function of normal random errors ε_x in x. The figure shows that the IL method underestimates the a-value, while the XIL stays accurate within RMSE less than 0.03 up to $\varepsilon_x=0.01$ (10% of $\tau=0.1$) and 0.05 at $\varepsilon_x=0.025$ (25% of $\tau=0.1$), as consistent with Eq. (10). Figure 6 and Table 2 compares results of IL and XIL

Atmospheric
Measurement
Techniques
Discussions
Open Access
EGU

methods with the following screening conditions applied to 38 sets of real Langley plot data at Tokyo University of Science (TUS) site for four months from February through May 2017:

$$m_2/m_1 \geq 2, \quad b(\text{SL}) < 10, \ 0.8 \leq b(\text{IL}), \text{ and } b(\text{XIL}) \leq 1.2, \ e_u(\text{IL}), \text{ and } e_u(\text{XIL}) \leq e_{u0}, \tag{17}$$

where m_1 and m_2 are lower and upper limits of airmass in the IL plot. The threshold residual ε_{u0} is given as 0.02, 0.03 and

5   0.05. The figure and table indicate that the a-value from SL is largely scattered, suggesting determination of F_0 by SL at turbid sites like Tokyo is not recommendable. On the other hand, a-values from IL and XIL converge on a regression line within differences of 2-3%, with a tendency of systematically smaller values by IL than those from XIL method by amounts of ε_{u0} and $\varepsilon_{u0}/2$, respectively. Although the difference between IL and XIL is not large as far as we select low noise data, we would like to recommend the XIL method to be applied to 5 to 10 Langley plot data sets in order to secure the accuracy of

10   1% to 2% in F_0 using the screening conditions of Eq. (17). The figure also shows that we can detect a long-term decreasing trend of a-value by about 10% during the period at the TUS site.

4. Sky radiance calibration for the sky radiometer

Several methods have been proposed for on-site calibration of the sky radiance measured by the sky radiometer, such as solar disk scan method, point-source method or lamp scan method, and diffuse plate method (Nakajima et al., 1986, 1996;

15   Boi et al., 1999). Among them, the solar disk scan method has been routinely used in the SKYNET measurement of the SVA of the sky radiometer by scanning a circumsolar domain (CSD) of ±1° by ±1° around the sun with every 0.1° interval.

The irradiance received by the radiometer, which is aimed at the direction (x, y) in a Cartesian coordinate system of angular distance from the center of the solar disk at origin ($x=0, y=0$), is an angular integration of radiances weighted by the response function of the radiometer f_R in the field of view (FOV),

20

$$F(x,y) = \iint\limits_{FOV} dx' \, dy' f_R(x'-x, y'-y) L(x',y') \ . \tag{18}$$

In the case of diffuse sky radiance measurement, the SVA of the radiometer is given from Eqs. (1) and (18) as,

$$\Delta\Omega = \iint\limits_{FOV} dx' \, dy' f_R(x', y') \ . \tag{19}$$

In the case of the solar disk scan, the main term for F is given as follows under conditions of small contribution from diffuse sky radiation in the CSD,

25

$$F(x,y) = \iint\limits_{FOV} dx' \, dy' f_R(x'-x, y'-y) L_d(x',y') \ , \tag{20a}$$

where L_d is the radiance distribution of the solar disk. The angular aperture of the sky radiometer is about 1°, whereas the solar disk radius is about 0.5°, so that we can measure the solar disk-averaged value of the radiometer response function as,

9

$$\overline{f}_R(x,y) = \frac{F(x,y)}{F_d} \; . \tag{20b}$$

From Eqs. (1), (20a) and (20b), the following normalization condition has to be fulfilled,

$$\overline{f}_R(0,0) = 1 \; . \tag{20b}$$

The SVA can be obtained by the angular integration of the radiance in the CSD as,

$$I \equiv \iint_{CSD} dx\,dy\,\overline{f}_R(x,y) = \frac{1}{F_d} \iint_{CSD} dx\,dy \iint_{FOV} dx'\,dy'\,f_R(x'-x,\,y'-y)L_d(x',y')$$

$$= \frac{1}{F_d} \iint_{FOV} dx'\,dy'\,L_d(x',y') \iint_{CSD} dx\,dy\,f_R(x'-x,\,y'-y) = \Delta\Omega \tag{20c}$$

The last expression is obtained by Eqs. (19) and Eq. (20c), if the size of CSD is large enough to include FOV or the contribution outside the CSD is small. These equations indicate flatness of the response function around the optical axis should be secured in manufacturing the sky radiometer for stable measurement of the direct solar radiation through Eq. (20b). The perfect flatness is realized by optics without an objective lens, which is useful for moving platform such as aircraft and ship (Nakajima et al., 1986).

Though not performed routinely, the lamp scan method has been performed for the current version of the sky radiometer (Manago et al., 2016). The merit of the method is that we can narrow the size of the point source below 0.5° and can extend the CSD size beyond ±1° without significant effect of the sky light. Analyzing data from the solar disk scan and lamp scan methods, Uchiyama et al., (2018b) found an underestimation of SVA from the disk scan method of 0.5 % to 1.9 % and proposed a correction method by extending CSD size up to scattering angle of 2.5° assuming an extrapolation function as illustrated in Fig. 7.

5. Retrievals of parameters for atmospheric constituents

Once the values of radiometer calibrataion constants, F_0 and SVA, are determined by the calibration methods described in the preceding two sections, the geophysical parameters of aerosols, clouds, water vapor and ozone are retrieved by inversion of F and/or R in Eqs. (2a) and (2c) at full or specific scattering angles (Fig. 3). Aerosol retrievals are done using Skyrad.pack version 4.2 or version 5. The former is based on inversion scheme of the Phillips-Twomey type solution of the first kind of Fredholm integral equation with homogeneous smoothing constraint and the latter is based on the second kind of the equation with inhomogeneous constraint with a priori climate data for aerosols (Twomey, 1963) to retrieve the inherent aerosol optical properties. The package adopts accurate yet fast IMS method for solar aureole radiance calculation (Nakajima and Tanaka, 1988) for full scalar radiative transfer calculation with polarization correction by Ogawa et al. (1989). A version of Meteorological Research Institute of Japan Meteorological Agency (MRI version) was also developed including non-spherical scattering kernel of Dubovik et al. (2006) (Kobayashi et al., 2010).

Che et al. (2008) reported that AOTs between sky radiometer (POM02) and Cimel sunphotometer at a Beijing site, China agreed within a relative AOT RMSD of about 1% without a large wavelength dependence, i.e. 0.91, 1.03, 0.82, 1.27 % at λ= 440, 670, 870, 1020nm, respectively, which corresponds to ε_τ= 0.005 for a representative optical airmass of 2 or σ_a= 0.6% in Eq. (10) for a representative AOT of 0.3 at the site. The value of the Ångström exponent agrees within 6% between 440nm

5 and 870nm and 1% between 500nm and 870nm.

SKYNET instruments are regularly compared with Precision Filter Radiometer (PFR) instruments belonging to the World optical depth Research and Calibration center (WORCC) and the Global Atmospheric Watch PFR network. Results of three POM instruments compared with the reference WORCC triad in 2015 showed differences less than 0.005 and 0.01 in all cases and for 500nm and 865 nm respectively during the 4th filter radiometer comparison (Kazadzis et al., 2018a). At the

10 same campaign Ångström exponent mean differences were less than 0.5. Since 2015 PFR vs POM long term comparisons have been performed at various stations, i.e. Valencia/Spain, Chiba/Japan, Davos/Switzerland and in the QUATRAM campaign (http://www.euroskyrad.net/quatram.html) at Rome/Italy.

Figure 8 shows comparisons of AOT at λ= 870nm from three radiometers, i.e. sky radiometer, Cimel sun-sky photometer and PMOD PFR (Khatri et al., 2016; Kazadzis et al., 2018a; personal communication by Campanelli). The figure indicates

15 ε_τ of about 0.01 is also consistent with the discussion regarding Eq. (11). The PFR comparison uses the result from SUNRAD pack (Estelles et at., 2012) where only direct measurements from the sky radiometer are used to retrieve AOT, having an higher time resolution with respect to direct measurement performed during the almucantar scenarios. During the comparison a 2-3% difference were found.

The SSA from SKYNET, on the other hand, was known to be overestimated as pointed by Che et al. (2008). Hashimoto et

20 al. (2012) and Khatri et al. (2016) studied error propagation from errors in F_0, SVA, ground albedo, cloud screening, and inversion algorithms. One possible reason of systematically large SSA by SKYNET is overestimation of the sky radiance due to underestimation of SVA as suggested by Eq. (1) in the solar disk scan method as described in the previous section. Another reason is a cloud contamination that causes overestimation of scattered radiation. Version 5 tends to be robust to the cloud contamination compared to version 4.2, owing to inversion constraints by a priori SDF which filters out cloud particles

25 necessary for the enhanced cloud-scattered radiation. This robustness of version 5 makes the inversion of the aerosol SDF robust to various noises as reported by Che et al. (2014) and Jiang et al. (2019) who demonstrated a clear aerosol bimodal size distribution over Beijing in China by using Skyrad.pack version 5. Reflecting these past studies, SYNET has been undertaking efforts to (1) introduce inhomogeneous constraints by version 5, (2) stricter cloud screening, and (3) correction of SVA underestimation (Khatri et al., 2010, 2016; Hashimoto et al., 2012; Uchiyama et al., 2018a, 2018b). In order to study

30 the consistency of retrieved parameters, sky radiometer users attended inter-comparison campaigns with other networks, like the QUATRAM campaigns in 2017 and 2018 for comparing with PMOD PFR, AERONET sun-sky photometers, and Pandora AMP radiometers (www.euroskyrad.net/quatram.html) and the KORUS-AQ campaign in 2018 (Mok et al., 2018).

Figure 9 shows a KORUS-AQ comparison of SSA after these improvements with those of AERONET and Panodra in from April to August 2016 on the roof of the Science Hall, Yonsei University in Seoul, Korea. The figure indicates an agreement of SSA in a range of 0.015. One reservation about the SSA retrieval by version 5, though, is that it tends to underestimate the SSA due to underestimation of the coarse aerosols when the a priori SDF for constraint tends to be zero for radii larger than

5   10μm. Estellés et al. (2018) found similar underestimation of the coarse aerosols by version 5 compared to aircraft in-situ observations (Marenco et al., 2018; Ryder et al., 2018) for African dust events in the Sunphotometer Airborne Validation Experiment in Dust (SAVEX-D) campaign during 16-25 August 2015 as shown in Fig. 10. The figure indicates the version 4.2 retrieved coarse mode SDF similar to the observed one though the error bar is large.

Water vapor amount is retrieved from direct solar irradiance measurement in the 940nm channel. F_0-value in the water vapor

10   channel is retrieved by the modified Langley plot (ML or MLP) method based on the following OT formula in stead of Eq. (3),

$$y = \ln F_0 - a_g x \,, \tag{21a}$$

$$y = \ln F + m(\tau_a + \tau_R), \quad x = (m_g C_g)^{b_g} \,, \tag{21b}$$

where τ_a and τ_R are AOT and OT for molecular scattering, respectively, and C_g is the column-integrated burden of gaseous

15   species, i.e., precipitable water vapor amount W in this case; m_g is optical airmass for the gaseous species; a_g and b_g are two prescribed constants to approximate the beam transmittance due to the gaseous species; a_g can be regarded as an equivalent absorption coefficient for band-averaged absorption of the gaseous species. It is common to assume m_g to be as that of atmospheric air mass, i.e., $m_g = m$ in the water vapor case. The value of τ_a is obtained by an interpolation of the AOT spectrum retrieved from the non-gas absorption channels. There are two algorithms for the SKYNET analysis. One is to use

20   the measured spectral response function of the interference filter of the sky radiometer to prescribe values of a_g and b_g by the theoretical absorption calculation (Uchiyama et al., 2014). This method is similar to that of the AERONET method. The strong line absorption theory of the 930nm spectral band yields $b_g = 0.5$ (Goody and Yung, 1989) in Eq. (21b). However, there is some dependence of b_g on the vertical structure of the atmosphere, so that an improved method is proposed by Campanelli et al. (2010, 2014, 2018) to determine a_g and b_g values by a statistical regression technique of daily observation

25   data at the site. They obtained a range of b_g value as 0.53 to 0.61 as monthly mean values of three years from 2007 to 2009 at San Pietro Capofiume site (SPC; 44°23′N, 11°22′E, 11 m MSL), Italy, with some seasonal dependence. One complexity of this method, though, is a need for measurements of W for making the regression analysis. They used W either from radiosonde data or a proxy of W constructed from surface meteorological data of temperature and relative humidity. Figure 11 compares W by the two methods with GPS and AERONET retrievals in Tsukuba, Japan and Valencia, Spain for data

30   taken in 2011. The figure shows RMSD from validation data is less than 2 g/cm² by both the methods, with some systematic underestimation of the slope of the regression line of 10% in the former method.

In order to get rid of the F_0 retrieval process in the water vapor channel, Momoi et al. (2019) proposed a new method of using water vapor dependence of the relative radiance along the almucantar circle of the sky. Although this method has a

Atmospheric
Measurement
Techniques
Discussions
Open Access

limited range of retrievable W less than 2 g/cm^2, there is merit in using the value from the method, say W_{sky}, as a proxy of $C_g= W$ in Eq. (22b) to perform the MLP on site, similar to the IL method for the non-absorption channels, but with

$$x= T_d(W_{\text{sky}}), \tag{22}$$

instead of Eq. (21b).

5   The columnar ozone amount is retrieved from the direct solar irradiance measurement of 315 nm channel for the Huggins band. Khatri et al. (2014) determined the F_0-value by a ML method Eq. (22) assuming b_g=1 for ozone without a significant line absorption structure. The formula of m_g is given by Robinson (1966). In the F_0 determination process, they simultaneously obtained an optimal value of the equivalent ozone absorption coefficient a_g which bring the slope of the ML plot to unity using data of ozone column burden $C_g= U$ measured by the Dobson spectrometer. RMSD of the fitting for a

10   campaign data at Tsukuba site from 13 December, 2012 to 8 January, 2013 was 13 Dobson Unit (DU) as shown in Fig. 12. They also reported a large degradation of filter transmission in the ozone channel.

    Cloud microphysical properties have been obtained from diffuse sky radiance measurements from satellites (Nakajima and King, 1990). Similar approach can be applied to the ground-based radiance measurements. Chiu et al. (2010, 2012) retrieved cloud optical thickness (COT) and effective particle radius (CER) from AERONET data. SKYNET uses the POM02 sky

15   radiometer which has 1.6 μm and 2.2 μm channels (Kikuchi et al., 2006; Khatri et al., 2019). Figure 13 compares COT and CER retrieved from POM2 zenith observations at the three sites of Chiba, Fukue and Hedo combined with retrievals from Himawari-8/AHI satellite-borne imager in a period of October 2015 to December 2016. Satellite retrieval results were obtained by the Comprehensive Analysis Program for Cloud Optical Measurement (CAPCOM) (Nakajima and Nakajima, 1995) in the system of AMATERASS (Takenaka et al., 2011; Damiani et al., 2018). Geostationary satellite observation has a

20   merit of frequent time-matching with the ground-based observation. Figure 14 also compares the broad-band radiance at zenith measured by a ground-based pyrheliometer and with broad-band horizontal radiative flux measured by a pyranometer with those theoretically calculated using the cloud parameters from sky radiometer measurement. The figure indicates that the down-welling radiance at zenith was consistent between the two radiometers, but horizontal radiative flux were not well represented by the cloud optical properties retrieved from the sky radiometer at nadir. This fact suggests that the

25   inhomogeneity of cloud fields is a main source of differences between the cloud parameters obtained by the sky radiometer and satellite measurements. The Cloud effective particle radius (CER) is compared in Fig. 14 between sky radiometer and satellite measurements, which indicates large differences between the two measurements suggesting the cloud inhomogeneity should be taken into account in the comparison.

6. Conclusions

30   The SKYNET community has undertaken efforts in improving the on-site calibration system such that it is accurate enough to provide retrieved aerosol parameters comparable to those of other networks as proved by several comparison studies. An

estimate of the accuracy of AOT retrievals is given by Eq. (10) for the IL method and Eq. (13) by the SL method, which is comparable to a 10% of the average AOT at the site, if the number of data is in an order of $n = 100$. The accuracy of SSA retrieval is around 0.015 for conditions of AOT440 > 0.4. Other retrievals such as water vapor, ozone and cloud optical properties have been performed, but they still need more efforts in order to improve their quality on a robust processing.

5   There are several aims for the next step of the SKYNET to make its system more reliable and useful for the science community. There are several algorithms to be installed to the unified system, i.e., improved version of the disk scan method by Uchiyama. Water vapor results should be analyzed for selection of an optimal method. We want to pursue our on-site calibration system which is more sustainable with a relatively small budget. However, continuous comparison of on-site calibrations of our standard sky radiometer with:

10   - high mountain calibrations,

     - travelling standard instruments,

     - and participation in small or large scale inter-comparison programs with other networks, under variable aerosol conditions,

are needed in order to continue verifying the on-site calibration quality.

Atmospheric
Measurement
Techniques
Discussions

References

Ångström, A. K.: Techniques of determining the turbidity of the atmosphere, Tellus, 13, 214-223, 1961.

Ångström, A. K.: Circumsolar sky radiation and turbidity of the atmosphere, Appl. Opt., 13, 474-477, 1974.

Boi, P., Tonna, G., Dalu, G., Nakajima, T., Olivieri, B., Pompei, A., Campanelli, M., and Rao, R.: Calibration and data
5   elaboration procedure for sky irradiance measurements, Appl. Opt., 38, 896–907, doi:10.1364/AO.38.000896, 1999.

Box, M. A., and Deepak, A.: Single and multiple scattering contributions to circumsolar radiation, Appl. Opt., 17, 3794-3797, 1978.

Box, M. A., and Deepak, A.: Retrieval of aerosol size distributions by inversion of simulated aureole data in the presence of multiple scattering, Appl. Opt., 18, 1376-1382, 1979.

10   Campanelli, M., Nakajima, T., and Olivieri, B.: Determination of the solar calibration constant for a sun sky radiometer. Proposal of an in situ procedure, Appl. Opt., 43, 651-659, 2004.

Campanelli, M., Estellés, V., Tomasi, C., Nakajima, T., Malvestuto, V., and Martínez-Lozano, J. A.: Application of the SKYRAD improved Langley plot method for the in situ calibration of CIMEL sun-skphotometers, Appl. Opt., 46, 2688-2702, 2007.

15   Campanelli, M., Lupi, A., Nakajima, T., Malvestuto, V., Tomasi, C., and Estelles, V.: Summertime columnar content of atmospheric water vapor from ground-based Sun-sky radiometer measurements through a new in situ procedure, J. Geophys. Res., 115, D19304, doi:10.1029/2009JD013211, 2010.

Campanelli, M., Estelles, V., Smyth, T., Tomasi, C., Martinez-Lozano, M. P., Claxton, B., Muller, P., Pappalardo, G. , Pietruczuk, A., Shanklin, J., Colwell, S., Wrench, C., Lupi, A., Mazzola, M., Lanconelli, C., Vitale, V., Congeduti, F.,
20   Dionisi, D., Cardillo, F., Cacciani, M., Casasanta, G., and Nakajima, T.: Monitoring of Eyjafjallajokull volcanic aerosol by the new European Skynet Radiometers (ESR) network, Atmos. Environ., 48, 33-45, doi: 10.1016/j.atmosenv.2011.09.070, 2012.

Campanelli, M., Nakajima, T., Khatri, P., Takamura, T., Uchiyama, A., Estelles, V., Liberti, G. L., and Malvestuto, V.: Retrieval of characteristic parameters for water vapour transmittance in the development of ground based Sun-Sky
25   radiometeric measurements of columnar water vapour, Atmos. Meas. Tech., 7, 1075–1087, doi:10.5194/amt-7-1075-2014, 2014.

Campanelli, M., Mascitelli, A., San`o, P., Diémoz, H., Estellés, V., Federico, S., Iannarelli, A. M., Fratarcangeli, F., Mazzoni, A., Realini, E., Crespi, M., Bock, O., Martínez-Lozano, J. A., and Dietrich, S.: Precipitable water vapour content from ESR/SKYNET sun-sky radiometers: validation against GNSS/GPS and AERONET over three different sites in Europe,
30   Atmos. Meas. Tech., 11, 81-94, 2018.

Che, H., Shi, G., Uchiyama, A., Yamazaki, A., Chen, H., Goloub, P., and Zhang, X.: Intercomparison between aerosol optical properties by a PREDE skyradiometer and CIMEL sunphotometer over Beijing, China, Atmos. Chem. Phys., 8, 3199–3214, doi:10.5194/acp-8-3199-2008, 2008.

Atmospheric
Measurement
Techniques
Discussions

Che, H., Shi, G., Zhao, H., Nakajima, T., Khatri, P., Takamura, T., Wang, H., Wang, Y., Sun, J., and Zhang, X.: Aerosol optical properties retrieved from a Prede sky radiometer over an urban site of Beijing, China, J. Meteorol. Soc. Japan, 92A, 17–31, doi: 10.2151/jmsj.2014-A02, 2014.

Chiu, J.-C, Huang, C.-H., Marshak, A., Slutsker, I., Giles, D. M., Holben, B., Knyazikhin, Y., and Wiscombe, W.: Cloud
5   optical depth retrievals from the Aerosol Robotic Network (AERONET) cloud mode observations, J. Geophys. Res., 115, doi 10.1029/2009JD013121, 2010.

Chiu, J. C., Marshak, A., Huang, C.-H., Várnai, T., Hogan, R. J., Giles, D. M., Holben, B. N., O'Connor, E. J., Knyazikhin, Y., and Wiscombe, W. J.: Cloud droplet size and liquid water path retrievals from zenith radiance measurements: examples from the Atmospheric Radiation Measurement Program and the Aerosol Robotic Network, Atmos. Chem. Phys., 12,
10   10313-10329, https://doi.org/10.5194/acp-12-10313-2012, 2012, 2012.

Damiani, A., Irie, H., Horio, T., Takamura, T., Khatri, P., Takenaka, H., Nagao, T., Nakajima, T. Y., and Cordero, R. R.: Evaluation of Himawari-8 surface downwelling solar radiation by ground-based measurements, Atmos. Meas. Tech., 11, 2501-2521, 2018.

Dave, J. D.: Determination of size distribution of spherical polydispersions using scattered radiation data, Appl. Opt., 10,
15   2035-2044, 1971.

Deirmendjian, D.: Theory of the solar aureole Part I: Scattering and radiative transfer, Annales de Géophysiqu, 13, 286-306, 1957.

Deirmendjian, D.: Theory of the solar aureole Part II: Applications to atmospheric models, Annales de Géophysiqu, 15, 218-249, 1959.

20   Dubovik, O., and King, M. D.: A flexible inversion algorithm for retrieval of aerosol optical properties from Sun and sky radiative measurements, J. Geophys. Res., 105, 20673–20696, 2000.

Dubovik, O., Smirnov, A., Holben, B., King, M. D., Kaufman, Y. J., Eck, T. F., and Slutsker, I.: Accuracy assessment of aerosol optical properties retrieval from Aerosol Robotic Net- work (AERONET) Sun and sky radiance measurements, J. Geophys. Res., 105, 9791–9806, 2000.

25   Dubovik, O., Holben, B., Eck, T. F., Smirnov, A., Kaufman, Y. J., King, M. D., Tanré, D., and Slutsker, I.: Variability of absorption and optical properties of key aerosol types observed in worldwide locations, J. Geophys. Res., 59, 590-608, 2002.

Dubovik, O., Sinyuk, A., Lapyonok, T., Holben, B. N., Mishchenko, M., Yang, P., Eck, T. F., Volten, H., Munõz, O., Veihelmann, B., van der Zande, W. J., Leon, J. F., Sorokin, M., and Slutsker, I.: Application of spheroid models to account for aerosol particle nonsphericity in remote sensing of desert dust, J. Geophys. Res., 111, D11208, 2006.

30   Eiden, R.: Calculations and measurements of the spectral radiance of the solar aureole, Tellus, 20, 380-399, 1968.

Estellés, V., Campanelli, M., Smyth, T. J., Utrillas, M. P., and Martínez-Lozano, J. A.: AERONET and ESR sun direct products comparison performed on Cimel CE318 and Prede POM01 solar radiometers, Atmos. Chem. Physics Discuss. 12, 4341-4371, doi:10.5194/acpd-12-4341-2012, 2012.

Estellés, V., Marenco, F., Ryder, C., Segura, S., O'sullivan, D., Brooke, J., Campanelli, M., Buxmann, J., and Martínez-Lozano, J. A.: Validation of AERONET and ESR/SKYNET size distributions with airborne insitu measurements in dust conditions. 9th International Workshop on Sand/Duststorms and Associated Dustfall, 22-24 May, Tenerife, Spain, 2018.

5   Green, A. E. S., Deepak, A., and Lipofsky, B.J.: Interpretation of the sun's aureole based on atmospheric models, Appl. Opt., 10, 1263-1279, 1971.

Goody, R.M. and Yung, Y.L.: Atmospheric Radiation, Second ed., Oxford Univ. Press, New York, Oxford., 286pp, 1989.

Hashimoto, M., Nakajima, T., Dubovik, O., Campanelli, M., Che, H., Khatri, P., Takamura, T., and Pandithurai, G.: Development of a new data processing method for the SKYNET skyradiometer observation, Atmos. Meas. Tech., 5, 10   2723-2737, doi:10.5194/amt-5-2723-2012, 2012.

Holben, B. N., Eck, T. F., Slutsker, I., Tanre´, D., Buis, J. P., Set- zer, A., Vermote, E., Reagan, J. A., Kaufman, Y. J., Nakajima, T., Lavenu, F., Jankowiak, I., and Smirnov, A.: AERONET – A federated instrument network and data archive for aerosol characterization, Remote Sens. Environ., 66, 1–16, 1998.

Hoyt, D. V.: The Smithsonian Astrophysical Observatory solar constant program, Rev. Geophys. Space Phys., 17, 427-458, 15   1979a.

Hoyt, D. V.: Pyrheliometric and circumsolar sky radiation measurements by the Smithsonian Astrophysical Observatory from 1923 to 1954, Tellus, 31, 217-229, 1979b.

Jiang, Z., Duan, M., Che, H., Zhang, W., Nakajima, T., Hashimoto, M., Chen, B., and Yamazaki, A.: Inter-comparison between the Aerosol Optical Properties Retrieved by Different Inversion Methods from SKYNET Sky Radiometer 20   Observations over Qionghai and Yucheng in China, Atmos. Meas. Tech. Discuss., https://doi.org/10.5194/amt-2019-39, in review, 2019

Kazadzis, S., Kouremeti, N., Diémoz, H., Gröbner, J., Forgan, B. W., Campanelli, M., Estellés, V., Lantz, K., Michalsky, J., Carlund, T., Cuevas, E., Toledano, C., Becker, R., Nyeki, S., Kosmopoulos, P.G., Tatsiankou, V., Vuilleumier, L., Denn, F. M., Ohkawara, N., Ijima, O., Goloub, P., Raptis, P.I., Milner, M., Behrens, K., Barreto, A., Martucci, G., Hall, E., Wendell, 25   J., Fabbri, B.E., and Wehrli, C.: Results from the Fourth WMO Filter Radiometer Comparison for aerosol optical depth measurements, Atmos. Chem. Phys., 18, 3185-3201, https://doi.org/10.5194/acp-18-3185-2018, 2018a.

Kazadzis, S., Kouremeti, N., Nyeki, S., Gröbner, J., and Wehrli, C.: The World Optical Depth Research and Calibration Center (WORCC) quality assurance and quality control of GAW-PFR AOD measurements, Geosci. Instrum. Method. Data Syst., 7, 39-53, https://doi.org/10.5194/gi-7-39-2018, 2018b.

30   Khatri P., Takamura, T., Shimizu, A., and Sugimoto, N.: Spectral dependency of aerosol light-absorption over the East China Sea region, SOLA, 6, 1−4, doi:10.2151/sola.2010-001, 2010.

Khatri, P., Takamura, T., Yamazaki, A., and Uchiyama, A.: Use of 315 nm channel data of the sky radiometer to estimate the columnar ozone concentration: A preliminary study, J. Meteorol. Soc. Japan, 92A, 185-194, doi:10.2151/jmsj.2014-A12, 2014.

Atmospheric
Measurement
Techniques
Discussions

Khatri, P., Takamura, T., Nakajima, T., Estellés, V., Irie, H., Kuze, H., Campanelli, M., Sinyuk, A., Lee, S.-M., Sohn, B. J., Pandithurai, G., Kim, S.-W., Yoon, S. C., Martinez-Lozano, J. A., Hashimoto, M., Devara, P. C. S., and Manago, N.: Factors for inconsistent aerosol single scattering albedo between SKYNET and AERONET, J. Geophys. Res. Atmos., 121, 1859–1877, doi:10.1002/2015JD023976, 2016.

5   Khatri, P., Iwabuchi, H., Hayasaka, T., Irie, H., Takamura, T., Yamazakai, A., Damiani, A., Letu, H., and Kai, Q.: Retrieval of cloud properties from sky radiometer observed spectral zenith radiances, Atmos. Meas. Tech., 12, 6037-6047,doi:10.5194/amt-12-6037-2019.

Kikuchi, N., Nakajima, T., Kumagai, H., Kuroiwa, H., Kamei, A., Nakamura, R., and Nakajima, T. Y.: Cloud optical thickness and effective particle radius derived from transmitted solar radiation measurements: Comparison with cloud radar observations, J. Geophys. Res., 111, D07205, doi:10.1029/2005JD006363, 2006.

10   Kobayashi, E., Uchiyama, A., Yamazaki, A., and Kudo, R.: Retrieval of aerosol optical properties based on the spheroid model, J. Meteor. Soc. Japan, 88, 847-856, 2010.

Kobayashi, H., and Shiobara, M.: Development of new shipborne aureolemeter to measure the intensities of direct and scattered solar radiation on rolling and pitching vessel, Proc. SPIE 9640, Remote Sensing of Clouds and the Atmosphere XX, 9640, 1A 1-9, 2015.

15   Manago, N., Khatri, P., Irie, H., Takamura, T., and Kuze, H.: On the method of solid view angle calibration for SKYNET skyradiometers, 4th International SKYNET workshop, Rome, Italy, 2–4 March, 2016.

Marenco, F., Ryder, C., Estellés, V., O'Sullivan, D., Brooke, J., Orgill, L., Lloyd, G., and Gallagher, M.: Unexpected vertical structure of the Saharan Air Layer and giant dust particles during AER-D, Atmos. Chem. Phys., 18, 17655–17668, https://doi.org/10.5194/acp-18-17655-2018.

20   Mok, J., Krotkov, N.A., Torres, O., Jethva, H., Li, Z., Kim, J., Koo, J.-H., Go, S., Irie, H., Labow, G., Eck, T. F., Holben, B. N., Herman, J., Loughman, R. P., Spinei, E., Lee, S. S., Khatri, P., and Campanelli, M.: Comparisons of spectral aerosol single scattering albedo in Seoul, South Korea, Atmos. Meas. Tech., 11, 2295–2311, 2018.

Momoi, M., Kudo, R., Aoki, K., Mori, T., Miura, K., Okamoto, H., Irie, H., Shoji, Y., Uchiyama, A., Ijima, O., Takano, M., and Nakajima, T.: Development of an on-site self-calibration and retrieval methods of precipitable water vapor for sky-radiometer observations, Atmos. Meas. Tech., under review. , 2019

Nakajima, T., Tanaka, M., and Yamauchi, T.: Retrieval of the optical properties of aerosols from aureole and extinction data. Appl. Opt., 22, 2951-2959, 1983.

Nakajima, T., Tanaka, M., Hayasaka, T., Miyake, Y., Nakanishi, Y., and Sasamoto, K.: Airborne measurements of the optical stratification of aerosols in turbid atmospheres, Appl. Opt., 25, 4374-4381, 1986.

Nakajima, T., and Tanaka, M.: Algorithms for radiative intensity calculations in moderately thick atmospheres using a truncation approximation, J. Quant. Spectrosc. Radiat. Transfer, 40, 51-69, doi: 10.1016/0022-4073(88)90031-3, 1988.

Nakajima, T., Tonna, G., Rao, R., Kaufman, Y., and Holben, B.: Use of sky brightness measurements from ground for remote sensing of particulate polydispersions, App. Opt., 35, 2672-2686, doi: 10.1364/AO.35.002672, 1996.

Atmospheric
Measurement
Techniques
Discussions

Nakajima, T., Yoon, S.-C., Ramanathan, V., Shi, G.-Y., Takemura, T., Higurashi, A., Takamura, T., Aoki, K., Sohn, B.-J., Kim, S.-W., Tsuruta, H., Sugimoto, N., Shimizu, A., Tanimoto, H., Sawa, Y., Lin, N.-H., Lee, C.-T., Goto, D., and Schutgens, N.: Overview of the Atmospheric Brown Cloud East Asian Regional Experiment 2005 and a study of the aerosol direct radiative forcing in east Asia, J. Geophys. Res., 112, D24S91, doi:10.1029/2007JD009009, 2007.

5 Nakajima, T. Y., and Nakajima, T.: Wide-area determination of cloud microphysical properties from NOAA AVHRR measurements for FIRE and ASTEX regions, J. Atmos. Sci., 52, 4043-4059, doi: 10.1175/1520-0469(1995)052<4043:WADOCM>2.0.CO;2, 1995.

Ningombam, S.S., Bagare, S.P., Singh, R.B., Campanelli, M., Khatri, P., Dorjey, N.: Calibration of a Sky radiometer (Prede) using observations obtained from Hanle and Merak high-altitude stations, Atmos. Res., 143, 118–128, 2014.

10 Ogawa, H., Tanaka, M., and Nakajima, T.: A simple expression for the additional sky radiance produced by polarization effects, J. Meteor. Soc. Japan, 67, 877-888, 1989.

O'Neill, N. T. and Miller, J. R.: Combined solar aureole and solar beam extinction measurements. 1: Calibration considerations, Appl. Opt., 23, 3691-3696, 1984a.

O'Neill, N. T. and Miller, J. R.: Combined solar aureole and solar beam extinction measurements. 2: Studies of the inferred
15 aerosol size distribution, Appl. Opt., 23, 3697-3703, 1984b.

Ramanathan, V., Li, F., Ramana, M. V., Praveen, P. S., Kim, D., Corrigan, C. E., Nguyen, H., Stone, E. A., Schauer, J. J., Carmichael, G. R., Adhikary, B., and Yoon, S.C.: Atmospheric brown clouds: Hemispherical and regional variations in long range transport, absorption and radiative forcing, J. Geophys. Res., 112, D22S21, doi:10.1029/2006JD008124, 2007.

Robinson, N.: Solar Radiation, Elsevier, Amsterdam, 347pp, 1966.

20 Rodgers, C. D.: Inverse Method for Atmospheric Sounding, World Sci., Singapore, 256 pp, 2000.

Ryder, C.L., Marenco, F., Brooke, J.K., Estelles, V., Cotton, R., Formenti, P., McQuaid, J.B., Price, H.C., Liu, D., Ausset, P., Rosenberg, P. D., Taylor, J. W., Choularton, T., Bower, K., Coe, H., Gallagher, M., Crosier, J., Lloyd, G., Highwood, E. J., and Murray, B. J.: Coarse-mode mineral dust size distributions, composition and optical properties from AER-D aircraft measurements over the tropical eastern Atlantic, Atmos. Chem. Phys., 18, 17225–17257, 2018,
25 https://doi.org/10.5194/acp-18-17225-2018.

Shaw, G. E.: Error analysis of multi-wavelength sun photometry, Pure Appl. Geophys., 114, 390-395, 1976.

Song, H. J., Sohn, B. J., Chun, H. W., Chun, Y., and Lee, S. S.: Improved cloud screening method for the analysis of sky radiometer measurements and application to Asian dust detection, J. Meteorol. Soc. Japan, 92A, 167-183, 2014.

Takamura, T., Nakajima, T., and SKYNET community group: Overview of SKYNET and its activities, Opt. Pura Apl., 37,
30 3303–3308, 2004.

Takamura, T., Takenaka, H., Cui, Y., Nakajima, T. Y., Higurashi, A., Fukuda, S., Kikuchi, N., Nakajima, T., Sato, I., and Pinker, R. T.: Aerosol and cloud validation system based on SKYNET observations: Estimation of shortwave radiation budget using ADEOS-II/GLI data, J. Remote Sens. Japan, 29, 40-53, 2009.

Atmospheric
Measurement
Techniques
Discussions

EGU

Takamura, T., Khatri, P., Sohn, B. J., Tugjsuren, N., Tana, B., Campanelli, M., and Pandihurai, G.: Aerosol optical properties and aerosol direct effects over typical sites of SKYNET network. International Conference book on climate change in arid and semi-arid regions, 91-98, Ulaanbaatar, Mongolia, ISBN 978-99973-823-5-1, 2013.

Takenaka, H., Nakajima, T. Y., Higurashi, A., Higuchi, A., Takamura, T., Pinker, R. T., and Nakajima, T.: Estimation of
5   solar radiation using a neural network based on radiative transfer, J. Geophys. Res., 116, D08215, doi:10.1029/2009JD013337, 2011.

Tanaka, M., Nakajima, T., and Shiobara, M.: Calibration of a sunphotometer by simultaneous measurements of direct-solar and circumsolar radiations, Appl. Opt., 25, 1170-1176, 1986.

Tanré, D., Devaux, C., Herman, M. and Santer, R.: Radiative properties of desert aerosols by optical ground-based
10 measurements at solar wavelengths, J. Geophys. Res., 93, 14223-14231, 1988.

Tonna, G., Nakajima, T., and Rao, R.: Aerosol features retrieved from solar aureole data: A simulation study concerning a turbid atmosphere, Appl. Opt., 34, 4486-4499, 1995.

Twitty, J.T.: The inversion of aureole measurements to derive aerosol size distributions. J. Atmos. Sci., 32, 584-591, 1975.

Twomey, S.: On the numerical solution of Fredholm integral equations of the first kind by the inversion of the linear system
15 produced by quadrature, J. Ass. Comp. Mech., 10, 97-101, 1963.

Uchiyama, A., Yamazaki, A., and Kudo, R.: Column water vapor retrievals from sky radiometer (POM-02) 940 nm data, J. Meteorol. Soc. Japan, 92A, 195-203, 2014.

Uchiyama, A., Matsunaga, T., and Yamazaki, A.: The instrument constant of sky radiometer (POM-02) - Part 1: Calibration constant, Atmos. Meas. Tech., 11, 5363-5388, https://doi.org/10.5194/amt-11-5363-2018, 2018a.

20 Uchiyama, A., Matsunaga, T., and Yamazaki, A.: The instrument constant of sky radiometer (POM-02) - Part 2: Solid view angle, Atmos. Meas. Tech., 11, 5389-5402, https://doi.org/10.5194/amt-11-5363-2018, 2018b.

Uchiyama, A., Shiobara, M., Kobayashi, H., Matsunaga, T., Yamazaki, A., Inei, K., Kawai, K., and Watanabe, Y.: Nocturnal aerosol optical depth measurements with modified skyradiometer POM-02 using the moon as a light source, Atmos. Meas. Tech. Discuss., https://doi.org/10.5194/amt-2019-230, in review, 2019.

25 Volz, F. E.: Photometer mit Selen-Photoelement zur spektralen Messung der Sonnenstrahlung und zur Bestimmung der Wellenlängenabhängigkeit der Dunsttrübung, Arch. Me- teor. Geophys. Bioklimatol., B10, 100–131, 1959.

Volz, F. E.: Economical Multispectral Sun Photometer for Measurements of Aerosol Extinction from 0.44 μm to 1.6 μm and Precipitable Water, Applied Optics, 13, 1732-1733, 1974.

Weinman, J. A., Twitty, J. T., Browning, S. R., and Herman, B. M.: Derivation of phase functions from multiply scattered
30 sunlight transmitted through a hazy atmosphere, J. Atmos. Sci., 32, 577-583, 1975.

Atmospheric Measurement Techniques Open Access
Discussions
EGU

Table 1. Sites recognized by the International Skynet Committee.

Name	Owner	Country	Location (Lat)	Location (Lon)	Location (MSL, m)	Sub-net analyzers	ISDC
Halley	British Antarctic Survey	Antarctica	75.350S	26.340W	30 m	ESR	
Rothera	British Antarctic Survey	Antarctica	67.340S	68.080W	0m	ESR	
Showa	NIPR	Antarctica	69.006S	39.590E	30m	-	x
Chajnantor, Atacama	Universidad de Santiago de Chile	Chile	33.451S	70.686W	5100 m	ESR	
Beijing/CAMS	CMA	China	39.933N	116.317E	106m	CAMS	
Beijing/IAP	IAP-CAS	China	39.977N	116.381E	92m	CAS	
Dunhuang	IAP-CAS	China	40.146N	90.799E	1120m	CAS, Chiba-U	
Hefei	AIOFM-CAS	China	31.897N	117.173E	30m	CAS, U-Toyama	
Lanzhou	Lanzhou-U	China	35.570N	104.133E	1965m	Lanzhou-U	
Qionghai	IAP-CAS	China	19.230N	110.46E	24m	CAS	
Xi'an	XAUT	China	34.25N	108.983E	396.9m	XAUT	
Orleans	NIES	France	47.965N	2.113E	131m	Chiba-U	x
Lindemberg	Meteorologisches Obervatorium Lindenberg/Mark	Germany	52.209N	14.121E	120 m	ESR	
Amaravati	IMD	India	16.573N	80.358E	343m	IMD	
Aurangabad	IMD	India	19.876N	75.343E	568m	IMD	
Gangtok	IMD	India	27.339N	88.607E	1650m	IMD	
Guwahati	IMD	India	26.100N	91.580E	54m	IMD	
Hanle	Indian Institute of Astrophysics	India	32.779N	78.964E	4500m	IIAP, Chiba-U	x
Hyderabad	National Remote Sensing Agency, India	India	17.469N	78.486E	811m	IMD, U-Toyama	
Jaipur	IMD	India	27.175N	75.955E	431m	IMD	
Jodhpur	IMD	India	26.300N	73.020E	224m	IMD	
Kolkata	IMD	India	22.650N	88.450E	88m	IMD	
Merak	Indian Institute of Astrophysics	India	33.480N	78.360E	4258m	IIAP, Chiba-U	x
Minicoy	IMD	India	8.274N	73.050E	2m	IMD	
Nagpur	IMD	India	21.100N	79.050E	310m	IMD	
New Delhi/IITM	Indian Institute of Tropical Meteorology	India	28.629N	77.174E	240m	IMD, Chiba-U	
New Delhi/IMD	IMD	India	28.580N	77.210E	216m	IMD, U-Toyama	
New Delhi/NPL	National Physical Laboratory, India	India	28.637N	77.174E	223m	IMD, U-Toyama	
Port Blair	IMD	India	11.670N	92.720E	79m	IMD	
Puducherry	IMD	India	11.942N	79.808E	3m	IMD	
Pune/IITM	Indian Institute of Tropical Meteorology	India	18.537N	73.805E	559m	IMD, Chiba-U	
Pune/IMD	IMD	India	18.530N	73.850E	559m	IMD	
Raipur	IMD	India	21.251N	81.630E	298m	IMD	
Ranichauri	IMD	India	30.250N	78.080E	1800m	IMD	
Rohtak	IMD	India	28.830N	76.580E	214m	IMD	
Sagar	IMD	India	23.839N	78.738E	427m	IMD	
Trivandrum	IMD	India	08.480N	76.950E	60m	IMD	
Varanasi	IMD	India	25.300N	83.020E	90m	IMD	
Visakhapatnam	IMD	India	17.720N	83.230E	18m	IMD	
Aosta	ARPA-VDA	Italy	45.742N	7.357E	570 m	ESR	
Bologna	CNR-ISAC	Italy	44.650N	11.650E	8m	Chiba-U	
Bologna	CNR-ISAC	Italy	44.520N	11.340E	60m	Chiba-U	
Messina	Italian Air force	Italy	38.200N	15.500E	0m	ESR	
Monte Cimone	Italian Air force	Italy	44.190N	10.700E	2165 m	ESR	
Novara	Italian Air force	Italy	45.530N	8.670E	169 m	ESR	
Paganella	Italian Air force	Italy	46.110N	11.040E	2129 m	ESR	
Rome	CNR-ISAC	Italy	41.905N	12.548E	70.0m	ESR	
Sigonella	Italian Air force	Italy	37.405 N	14.919 E	30 m	ESR	
Vigna di Valle	Italian Air force	Italy	42.080N	12.210E	270 m	ESR	
Abashiri	U-Toyama	Japan	44.018N	144.280E	45m	U-Toyama	
Chiba	Chiba-U	Japan	35.625N	140.104E	21m	Chiba-U, U-Toyama	x
Etchujima	Tokyo Univ. Marine Sci.	Japan	35.664N	139.796E	35.0m	Chiba-U, U-Toyama	x
Fuji Hokuroku	AIST	Japan	35.433N	138.750E	1150m	Chiba-U, U-Toyama	x
Fukue	Chiba-U	Japan	32.752N	128.682E	80m	Chiba-U, U-Toyama	x
Fukuoka	Kyushu-U	Japan	33.524N	130.475E	28m	Chiba-U, U-Toyama	x
Fukuoka	MRI	Japan	33.552N	130.365E	31m	MRI	
Fussa	U-Toyama	Japan	35.751N	139.323E	141m	U-Toyama	
Hedo	Chiba-U	Japan	26.867N	128.248E	65m	Chiba-U, U-Toyama	x
Ishigaki	JMA	Japan	24.337N	124.164E	6m	JMA	x
Itabashi	Tokyo Kasei Univ.	Japan	35.775N	139.721E	70m	Chiba-U	
Jodo	U-Toyama	Japan	36.566N	137.606E	2839m	U-Toyama	
Kamiyukawa	U-Toyama	Japan	34.062N	135.516E	535m	U-Toyama	
Kanazawa	Kanazawa Institute of Technology	Japan	36.533N	136.629E	26m	U-Toyama	
Kofu	Chiba-U	Japan	35.650N	138.567E	300m	Chiba-U, U-Toyama	x
Minamitorishima	MRI	Japan	24.300N	153.970E	7m	MRI	
Minamitorishima /JMA	JMA	Japan	24.288N	153.983E	7m	JMA	x
Miyakojima	MRI	Japan	24.737N	125.327E	50m	MRI, Chiba-U	
Moshiri	NIES	Japan	44.366N	142.260E	288m	Chiba-U, U-Toyama	x
Nagasaki	Nagasaki-U	Japan	32.786N	129.865E	35m	Chiba-U, U-Toyama	
Okayama	AIST	Japan	34.664N	133.931E	13m	U-Toyama	
Osaka	Kinki-U	Japan	34.642N	135.587E	19m	Chiba-U, U-Toyama	
Saga	Saga-U, NIES	Japan	33.233N	130.283E	8m	Chiba-U	x
Sapporo/ILTS	U-Toyama	Japan	43.084N	141.339E	30m	U-Toyama	
Sapporo/ILTS,MRI	U-Toyama	Japan	43.084N	141.339E	30m	U-Toyama	
Sapporo/JMA	JMA	Japan	43.060N	141.329E	17m	JMA	x
Sendai	Tohoku-U	Japan	38.260N	140.840E	153m	Chiba-U, U-Toyama	x
Shigaraki	U-Toyama	Japan	34.854N	136.105E	295m	U-Toyama	
Suzu, Ishikawa	U-Toyama	Japan	37.451N	137.359E	15m	U-Toyama	
Takayama	Gifu-U	Japan	36.145N	137.423E	1420m	Chiba-U, U-Toyama	x
Takikawa	U-Toyama	Japan	43.547N	141.897E	40m	U-Toyama	
Toyama	U-Toyama	Japan	36.700N	137.187E	30m	U-Toyama	
Tsukuba	Tsukuba-U	Japan	36.114N	140.096E	27m	Chiba-U, U-Toyama	x
Tsukuba/MRI	MRI	Japan	36.056N	140.125E	30m	MRI	
Kagurazaka	Tokyo Univ. of Science	Japan	35.699N	139.741E	70m	-	
Mandargovi	Chiba-U	Mongolia	45.743N	106.264E	1393m	Chiba-U	x
Ulaanbaatar	MUST, Chiba-U	Mongolia	47.886N	106.906E	1350m	Chiba-U	x
Lauder	NIWA, NIES	New Zealand	45.038S	169.681E	370m	Chiba-U	x
Ny-Alesund	NIPR	Norway	78.930N	11.861E	50m	U-Toyama	x
Belsk	Polish Academy of Science	Poland	51.837N	20.792E	190m	ESR, U-Toyama	
Anmyon	SNU	Republic of Korea	36.517N	126.317E	45m	SNU, U-Toyama	
Kongju	Kongju National Univ.	Republic of Korea	36.280N	127.080E	70m	SNU, U-Toyama	
Seoul	SNU	Republic of Korea	37.460N	126.950E	150m	SNU, Chiba-U, U-Toyama	x
Yongin	Hankuk University of Foreign Studies	Republic of Korea	37.336N	127.268E	167m	SNU, U-Toyama	x
Yonsei	Yonsei-U	Republic of Korea	37.570N	126.980E	60m	SNU	x
Barcelona	Universitat de Barcelona	Spain	41.385N	2.118E	97 m	ESR	
Valencia-Burjassot	Universitat de Valencia	Spain	39.507N	0.420W	60 m	ESR, Chiba-U	
Bangkok	TMD	Thailand	13.667N	100.605E	60m	Chiba-U	
Phimai	Chiba-U	Thailand	15.184N	102.565E	212m	Chiba-U, U-Toyama	x
Sri-samrong	Chiba-U	Thailand	17.157N	99.867E	50m	Chiba-U, U-Toyama	
Cambridge	British Antarctic Survey	United Kingdom	52.215N	0.080E	30 m	ESR	
Cardington	Met-Office	United Kingdom	52.100N	0.421W	30 m	ESR	
London	University College London-UAO	United Kingdom	51.524N	0.131W	45 m	ESR	
Plymouth	Plymouth Marine Lab.	United Kingdom	50.366N	4.148W	0m	ESR	
Aurora, Colorado	AIST	USA	39.400N	104.500W	1674 m	ESR	
Golden	National Renewable Energy Laboratory	USA	39.740N	105.180W	1829 m	ESR	

Atmospheric
Measurement
Techniques

Open Access

EGU

Discussions

Table 2. Estimates a and b values at λ= 500nm and their RMSD values (σ_a, σ_b) in the F_0 retrieval by IL and XIL methods for ILP data at Tokyo University of Science (TUS) site for four months from February through May 2017. Results of three screening conditions of Eq. (17) with ε_{u0}= 0.05, 0.03, and 0.02 are listed.

ε_u= 0.05	a	σ_a	$-b$	σ_b
SL	-8.220	0.389	0.296	0.321
IL	-8.247	0.050	0.968	0.082
XIL	-8.219	0.069	1.035	0.117

ε_u= 0.03	a	σ_a	$-b$	σ_b
SL	-8.253	0.238	0.237	0.163
IL	-8.249	0.039	0.973	0.070
XIL	-8.233	0.039	1.019	0.073

ε_u= 0.02	a	σ_a	$-b$	σ_b
SL	-8.190	0.168	0.247	0.160
IL	-8.243	0.030	0.990	0.064
XIL	-8.233	0.031	1.025	0.075

5
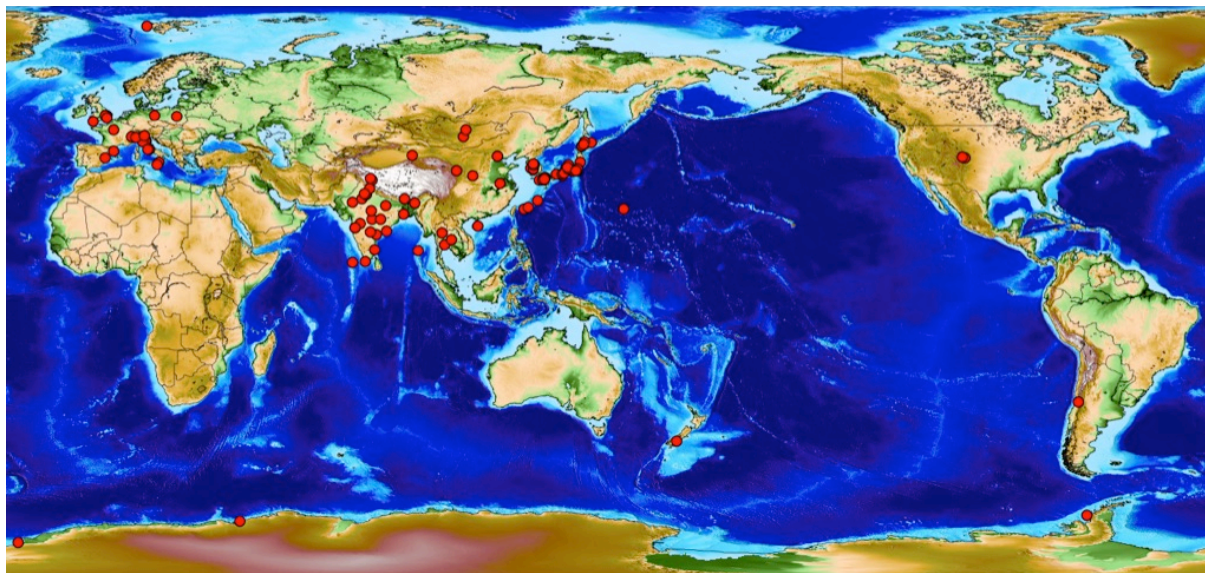
Figure 1: A map of the sky radiometer sites.

Atmospheric
Measurement
Techniques
Discussions
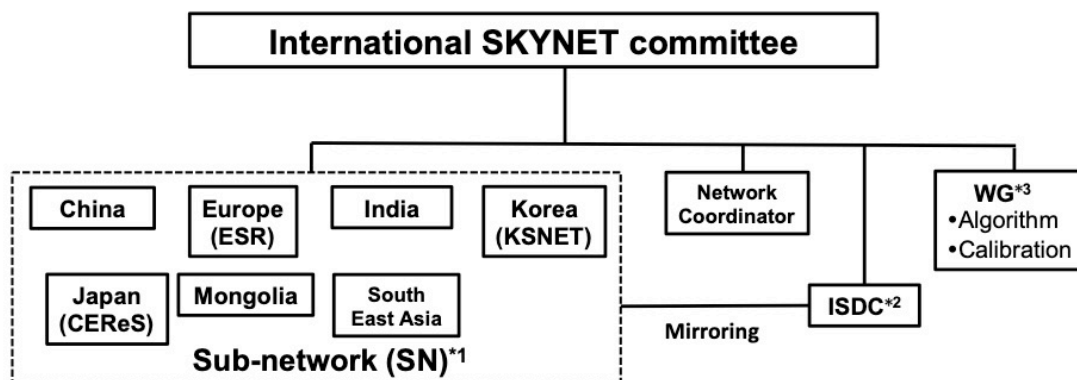
Figure 2: The structure of the International SKYNET committee.
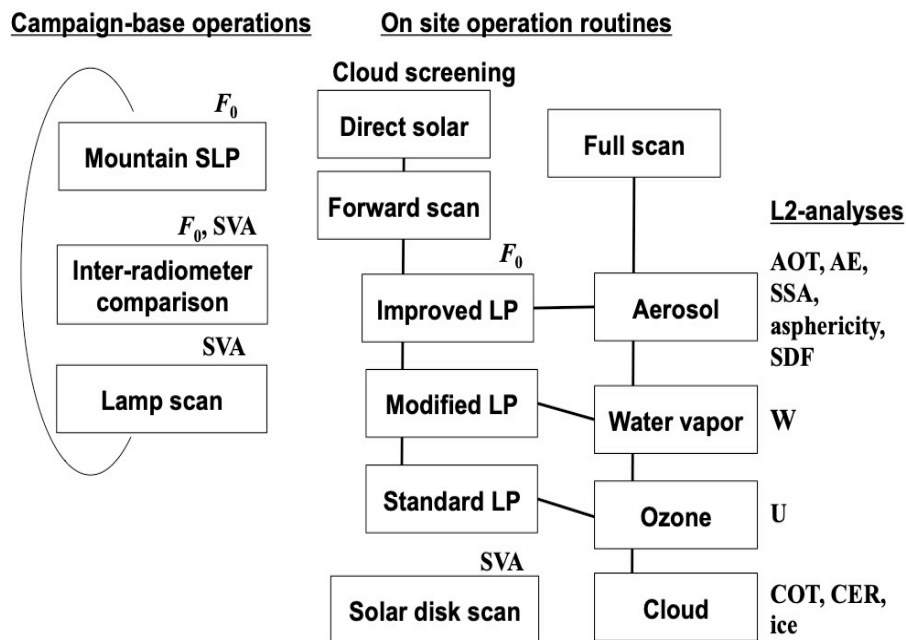
Figure 3: A flow chart of the SKYNET operation.

Atmospheric
Measurement
Techniques
Discussions
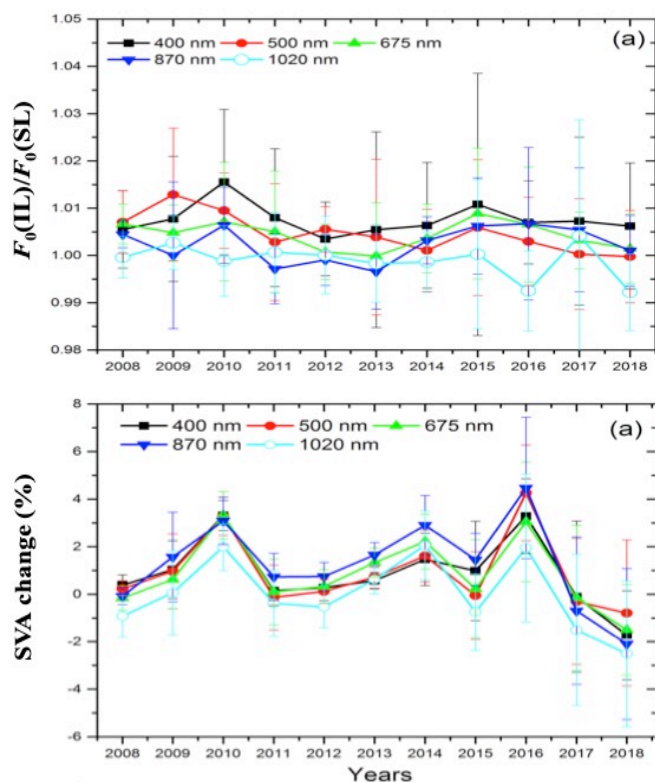
Figure 4: **Time series of the ratio of F_0-values from SL and IL methods (a) and SVA (b) from the observation taken by a single instrument (POM-01) at two pristine sites, IAO-Hanle during January 2008 - December 2010 and June 2015 - December 2018 and Merak during January 2011 - May 2015. The error bar indicates a representative monthly RMSD in each year.**

26
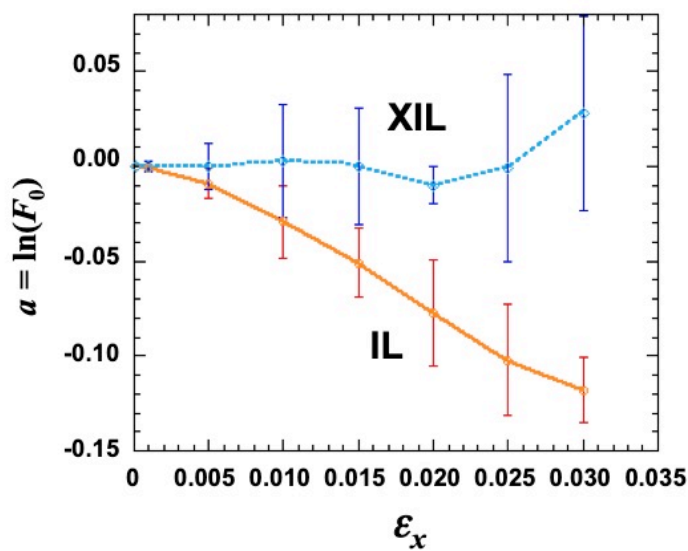
Figure 5: Retrieved values of $a = \ln(F_0)$ from IL and XIL methods with ten ensemble runs of an idealized experiment ($n=20$ and $m=1.3$ to 3.5) as a function of normal random error ε_x in x. True values are assumed as $F_0=1$, $\omega=1$, $\tau=0.1$.

Atmospheric
Measurement
Techniques
Discussions
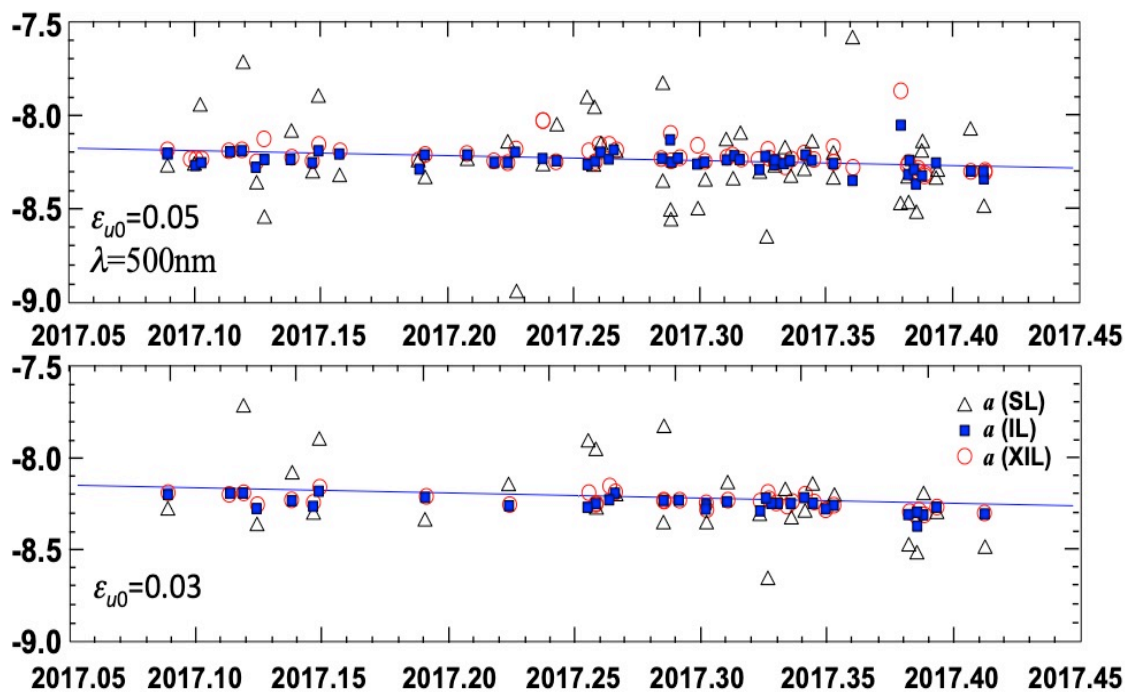
Figure 6: Time series of estimated *a*-values by IL and XIL methods for ILP data at Tokyo University of Science (TUS) site for four months from February through May 2017. Presented are results of two screening conditions of Eq. (17) with ε_{u0}= 0.05 and 0.03 at λ= 500nm.

Atmospheric
Measurement
Techniques
Discussions

Open Access

EGU
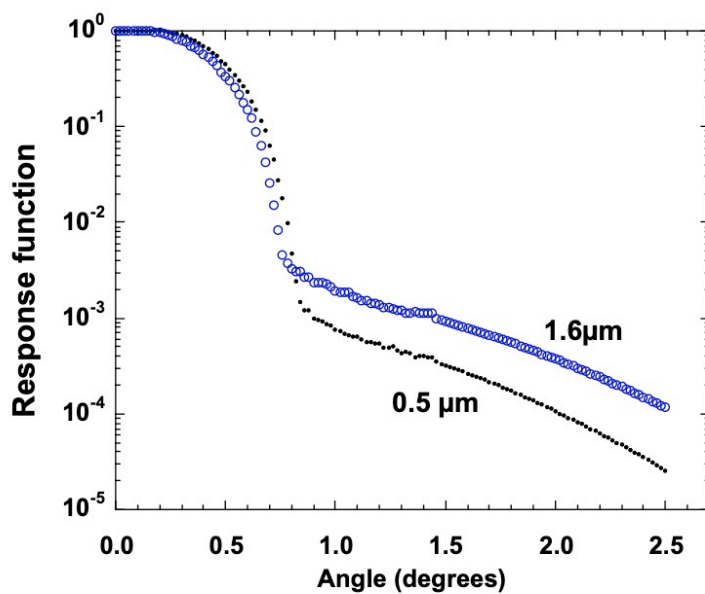
Figure 7: Response functions of the sky radiometer at λ= 0.5 μm and 1.6μm measured by the solar disk scan method.
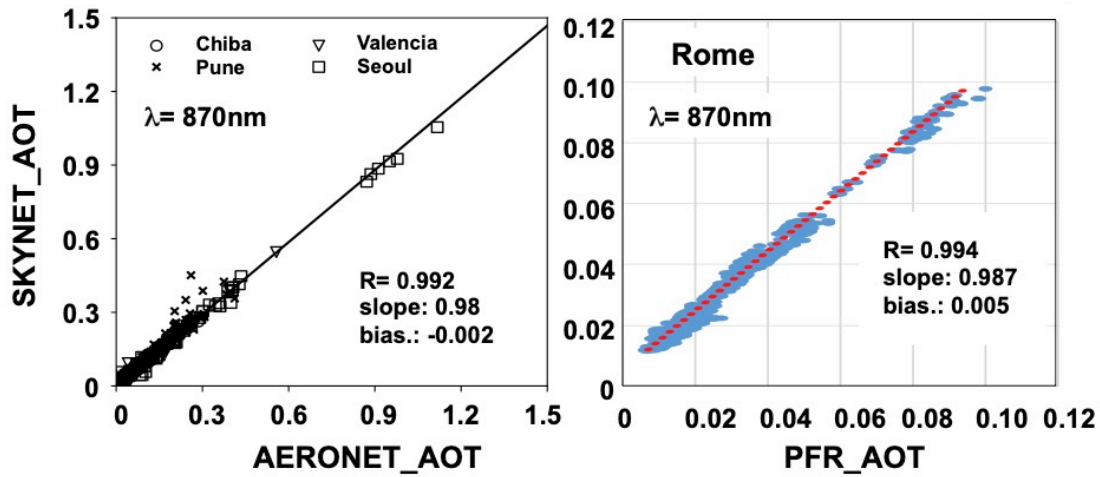
Figure 8: Comparison of AOT values at λ= 870nm obtained by sky radiometer, Cimel sun-sky photometer and PMOD PFR.
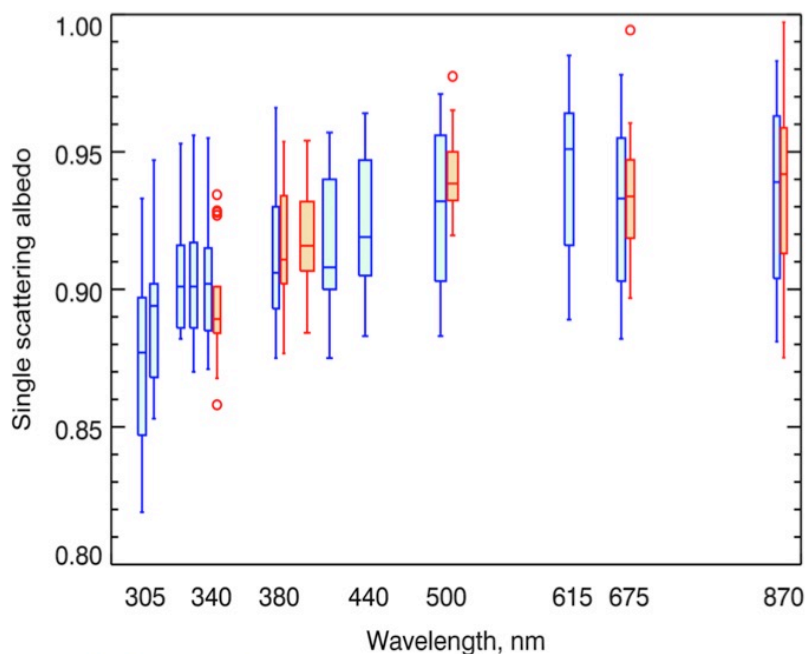
Figure 9: Combined spectral SSA from AMP-retrievals (blue symbols) and SKYNET retrievals (orange symbols) using MODIS-derived surface albedo. The bottom and top edges of the boxes are located at the sample 25th and 75th percentiles; the whiskers extend to the minimal and maximal values within 1.5 IQR. The outliers are shown in circles. The center horizontal lines are drawn at the median values. The whisker-boxes are computed using AOD440 ≥ 0.4 criteria to correspond the best quality level 2 AERONET data. Cited from Mok et al. (2018).

Atmospheric
Measurement
Techniques
Discussions
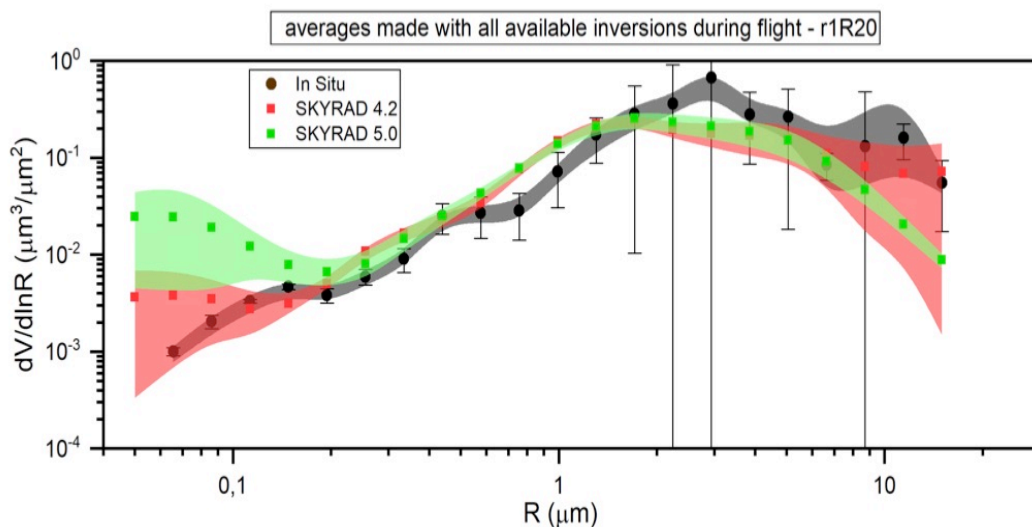
Figure 10: Retrieved and observed aerosol size distribution functions in the African dust event cases in the Sunphotometer Airborne Validation Experiment in Dust (SAVEX-D) campaign during 16-25 August 2015 (Estellés et al., 2018; Marenco et al., 2018; Ryder et al., 2018).
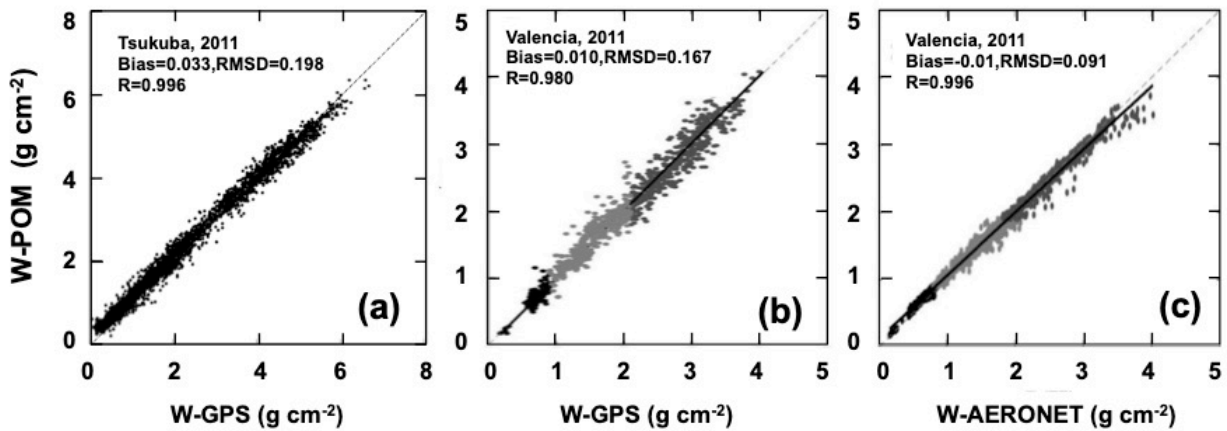
Figure 11: Precipitable water retrieved by Uchiyama et al. (2014) in panel (a) and by Campanelli et al. (2018) in panels (b) and (c).
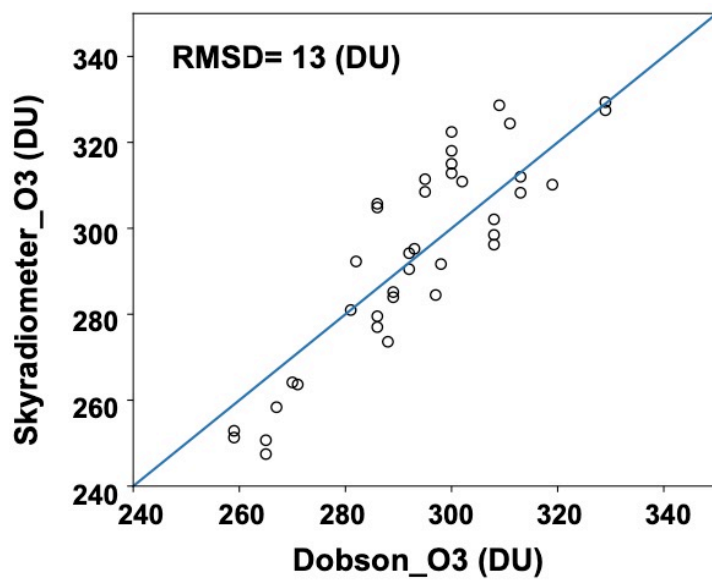
Figure 12: Comparison of column ozone amount (DU) retrieved from the sky radiometer at MRI Tsukuba-site and from Dobson spectrometer at JMA Tateno Observatory from 13 December, 2012 to 8 January, 2013.
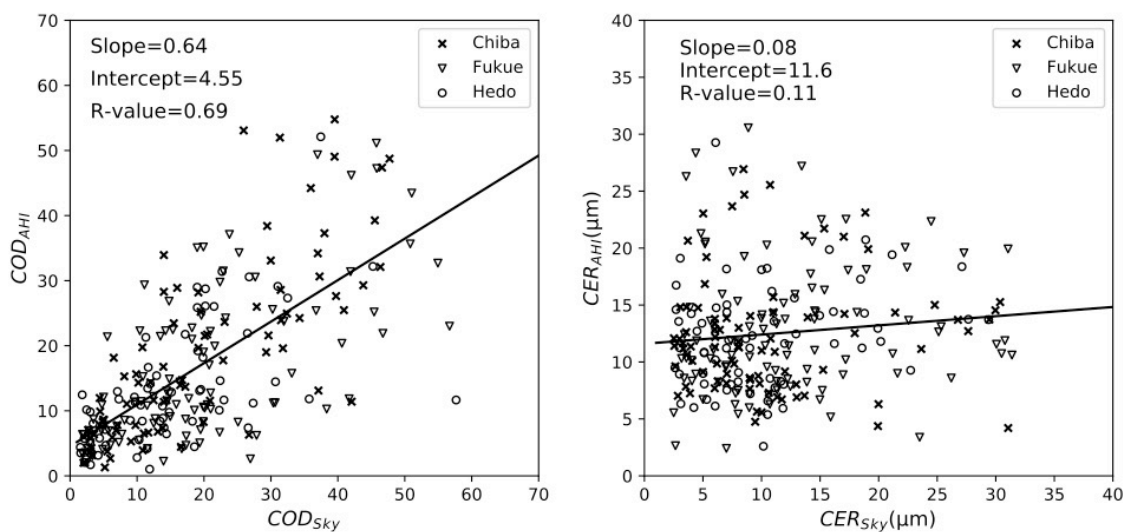
Figure 13: Comparison of cloud optical thickness (COT) and effective particle radius (CER) retrieved from sky radiometer at Chiba, Fukue and Hedo sites and Himawari-8/AHI satellite-borne imager in a period of October 2015 to December 2016 (Khatri et al., 2019).
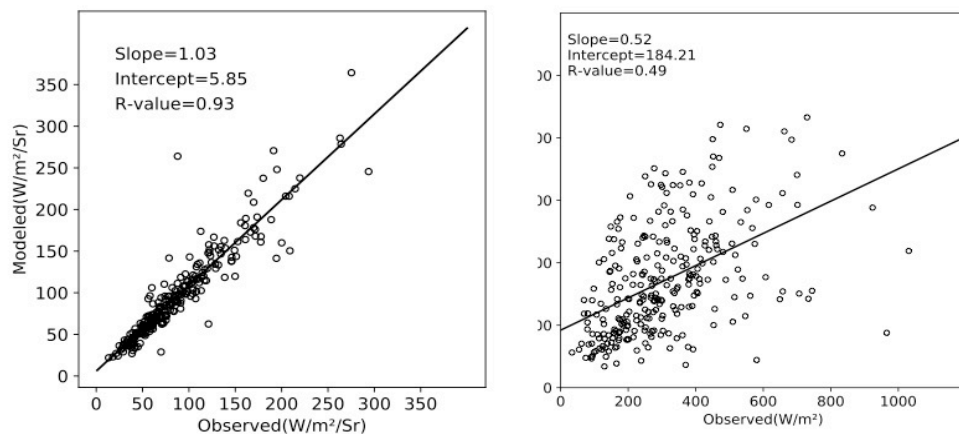
Figure 14: Same as in Fig. 13 but for comparison between modeled and observed broad-band (a) radiances and (b) irradiances for modeled values using sky radiometer cloud proprieties.